Microdynamic nature of lattice distortion and its effects on spin texture evolution behavior in skyrmion materials

Huaqing Wang,[1,2,3] Haohua Wen,[1,2,3,4,*] Yifeng Wu,[1,2,3] and Yue Zheng[1,2,3,†]

[1]*Guangdong Provincial Key Laboratory of Magnetoelectric Physics and Devices, School of Physics, Sun Yat-sen University, Guangzhou 510275, China*

[2]*State Key Laboratory of Optoelectronic Materials and Technologies, School of Physics, Sun Yat-sen University, Guangzhou 510275, China*

[3]*Centre for Physical Mechanics and Biophysics, School of Physics, Sun Yat-sen University, Guangzhou 510275, China*

[4]*Sino-French Institute of Nuclear Engineering and Technology, Sun Yat-sen University, Zhuhai 519082, China*

(Received 25 October 2023; revised 16 January 2024; accepted 27 February 2024; published 22 March 2024)

Spin-lattice coupling is one of the microdynamic sources of magnetic-mechanical effect, which can significantly affect the physical properties of materials hosting the skyrmion microstructure. Recent studies found a local lattice distortion is a natural result induced by the spin-lattice coupling and the nonalignment of spin texture, and it can lead to a non-Arrhenius transport behavior of skyrmion spin texture. In this paper, we study the deep insight of the microdynamic nature of this local lattice distortion field (LLDF). Starting with a general atomistic model for the chiral magnetic system containing the intrinsic spin-lattice coupling, we propose an analytical expression of the LLDF morphology. It suggests that the LLDF is an irrational strain-field with source, and is independent of the type of skyrmion spin texture, i.e., either Bloch- or Néel-type. The numerical simulations results based on spin-lattice dynamics support this conjecture. Subsequently, the effects of LLDF are discussed on the transport and stability of the skyrmion spin texture, which are two key issues for the skyrmion engineering and application. From the simulation results, the LLDF is found to bring the negative effects. The presence of LLDF, (1) brings a dragging force so to reduce the moving speed of spin texture for skyrmion transport and (2) enhances the thermal fluctuation of the spin-lattice-coupled system so to reduce the skyrmion lifetime. Our study provides an underlying mechanistic understanding on the control and manipulation of the magnetic skyrmion.

DOI: 10.1103/PhysRevB.109.104427

I. INTRODUCTION

Magnetic skyrmion (short for skyrmion in the rest) is a nanosize vortex spin texture observed in the magnetic materials with broken inversion symmetry [1]. Competition between Dzyaloshinskii-Moriya (DMI), Heisenberg exchange (HEI), Zeeman (ZI), and anisotropic magnetic (AMI) interactions is the most significant mechanism for the topologically stable skyrmion spin texture [2]. Since it can be driven by a low electric current density [3–5], the skyrmion is considered as a promising candidate for the information carrier in spintronic devices [6–13]. In the microdynamics, the atomic spins are attaching to their lattices, giving rise to the intrinsic spin-lattice coupling (SLC) [14,15], which is one of the microdynamic representations of the magnetic-mechanical coupling. In the skyrmion materials, the noncollinear spin texture will definitely lead to a corresponding LLDF owed to the SLC. Therefore, the thermodynamic and dynamical evolution of skyrmion spin texture is inevitably accompanied by the LLDF response. For instance, the magnetorestriction of a chiral magnet under the applied magnetic field is found to be the accumulative result of the LLDF [16–19]. In addition, because the stochastic motion of LLDF exerts a conservative potential, the skyrmion spin texture shows the nonlinear transport behaviors through the intrinsic SLC [14–16]. In this regard, in the thermodynamic and dynamical points of view, spin texture and LLDF are both sides of the "coin" of skyrmion (see Fig. 1). Due to the SLC, we can find that either a Bloch [see Fig. 1(c)] or Néel spin texture [see Fig. 1(e)] results in a radical expanding LLDF in Fig. 1(d). In other words, a rotational passive magnetization field $\{\boldsymbol{S}_i\}$ is accompanied by an irrotational LLDF $\varepsilon(\boldsymbol{r})$ with source. In this paper, we aim to get the deep insight of the microdynamic feature of the LLDF and its effects so to get the comprehensive understanding of the thermodynamic and dynamical responses of skyrmion spin texture.

The structure of the paper is as follows: The theoretical model of LLDF and the detailed derivation of the LLDF morphology will be introduced in Sec. II, and the results and discussion about the effects of LLDF on skyrmion transport and stability will presented in Sec. III, following which the conclusions are drawn in Sec. IV.

II. THEORETICAL MODEL

In this section, we will show the analytical expression for the morphology of the LLDF induced by the SLC and spin spiral magnetic configuration, starting with an atomistic Hamiltonian of a coupled dynamics system of spin and lattice.

*Corresponding author: wenhh3@mail.sysu.edu.cn

†Corresponding author: zhengy35@mail.sysu.edu.cn

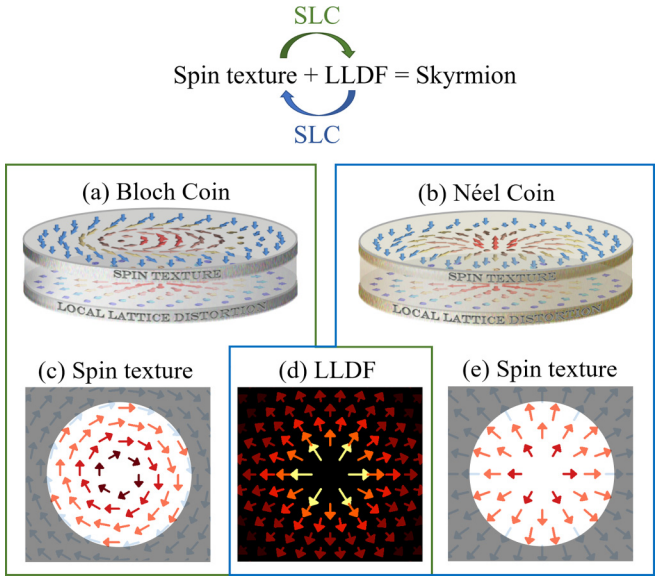

FIG. 1. The conceptual pictures of (a) Bloch coin and (b) Néel coin. Front side is spin texture, and back side is LLDF, bonded by the intrinsic spin-lattice coupling. Under the (c) Bloch spin texture and (d) Néel spin texture is (e) the same morphology of LLDF, which is an irrotational field.

A. A general expression of interatomic force

In microdynamics, a chiral magnetic material can be regarded as an ensemble of N interactive particles having the spin $\boldsymbol{S}_i$ and the lattice $\boldsymbol{r}_i$, $\boldsymbol{p}_i$ degrees of freedom, whose Hamiltonian $\mathcal{H}$ generally reads

$$\mathcal{H} = \mathcal{H}_L(\{\boldsymbol{r}_i, \boldsymbol{p}_i\}) + \mathcal{H}_S(\{\boldsymbol{S}_i\}) \tag{1}$$

Here, $\mathcal{H}_L$ describes the lattice dynamic as

$$\mathcal{H}_L = \sum_{i=1}^{N} \frac{\boldsymbol{p}_i^2}{2m_i} + U(\{\boldsymbol{r}_i\}) \tag{2}$$

with m_i, $\boldsymbol{p}_i$, and $\boldsymbol{r}_i$ as the ith atomic mass, momentum, and position, respectively. $U(\{\boldsymbol{r}_i\})$ describes the nonmagnetic interaction. The spin dynamics $\mathcal{H}_S$ is consist of the HEI, DMI, and ZI, as

$$\begin{aligned}\mathcal{H}_S &= \mathcal{H}_J + \mathcal{H}_D + \mathcal{H}_Z \\ &= \sum_{i<j} J(r_{ij})\boldsymbol{S}_i \cdot \boldsymbol{S}_j - \sum_{i<j} D(r_{ij})\hat{\boldsymbol{r}}_{ij} \cdot \boldsymbol{A}_{ij} - \boldsymbol{H}_{\text{ext}} \cdot \sum_i \boldsymbol{S}_i.\end{aligned} \tag{3}$$

Here, $\boldsymbol{S}_i$ is the ith atomic spin vector. In order to simplify our discussion, we assume that the length of each spin is unity as $|\boldsymbol{S}_i| = 1$. $\boldsymbol{r}_{ij} = \boldsymbol{r}_i - \boldsymbol{r}_j$ is the atomic displacement from the jth atom to the ith atom, and $r_{ij} = |\boldsymbol{r}_{ij}|$ represents the atomic distance, and $\hat{\boldsymbol{r}}_{ij}$ is the unit vector as $\hat{\boldsymbol{r}}_{ij} = \boldsymbol{r}_{ij}/r_{ij}$. $J(r_{ij})$ and $D(r_{ij})$ are respectively the HEI and DMI strengths, as the functions of the atomic distance r_{ij} to represent the scalar SLC [20,21]. Notably, $\boldsymbol{A}_{ij}$ in the bulk magnets (supporting the Bloch skyrmion [22–24]) is different from that in the interface of ferromagnetic layer and heavy metal (supporting the Néel skyrmion [13,25–27]), respectively defined as

$$\boldsymbol{A}_{ij} = \begin{cases} \boldsymbol{S}_i \times \boldsymbol{S}_j, & \text{for } b\text{DMI} \\ \hat{z} \times (\boldsymbol{S}_i \times \boldsymbol{S}_j), & \text{for } i\text{DMI} \end{cases} \tag{4}$$

where $\hat{z}$ is the normal unit vector of the interface. In the general study of skyrmion, an anisotropic magnetic energy is considered to be an important factor for stabilizing the skyrmion spin texture, written in terms of $-K_U(S_i^z)^2$ [28], for example. For the spin dynamics, such an anisotropic energy provides an effective magnetic field along $\hat{z}$ direction, which acts the same as an applied external field as $\boldsymbol{H}_{\text{ext}} = H_{\text{ext}}\hat{z}$ in current model of Eq. (1). In this case, excluding the anisotropic energy will not give rise to significant physical effects in current issue.

From the Hamiltonian $\mathcal{H}$ in Eq. (1) for the spin-lattice coupled system, the interatomic force $\boldsymbol{f}_{ij}$ between the ith and jth atoms is derived as (see detailed deduction in Appendix)

$$\boldsymbol{f}_{ij} = -\frac{\partial U}{\partial r_{ij}}\hat{\boldsymbol{r}}_{ij} + \frac{\partial J}{\partial r_{ij}}\boldsymbol{\varphi}_{ij} + \frac{\partial D}{\partial r_{ij}}\boldsymbol{A}_{ij}^{\parallel} + \frac{D}{r_{ij}}\boldsymbol{A}_{ij}^{\perp}, \tag{5}$$

where $\boldsymbol{\varphi}_{ij} \equiv \hat{\boldsymbol{r}}_{ij}(\boldsymbol{S}_i \cdot \boldsymbol{S}_j)$; $\boldsymbol{A}_{ij}^{\parallel}$ and $\boldsymbol{A}_{ij}^{\perp}$ are respectively the $\boldsymbol{A}_{ij}$ components parallel and perpendicular to the reference direction $\hat{\boldsymbol{r}}_{ij}$, and

$$\boldsymbol{A}_{ij}^{\parallel} = (\hat{\boldsymbol{r}}_{ij} \cdot \boldsymbol{A}_{ij})\hat{\boldsymbol{r}}_{ij} \text{ and } \boldsymbol{A}_{ij}^{\perp} = (\hat{\boldsymbol{r}}_{ij} \times \boldsymbol{A}_{ij}) \times \hat{\boldsymbol{r}}_{ij}. \tag{6}$$

According to Eq. (5), the spin texture denoted by $\{\boldsymbol{S}_i\}$ significantly affects the interatomic force $\boldsymbol{f}_{ij}$, thus the stable lattice microstructure denoted by $\{\boldsymbol{r}_i\}$. In particular, the magnetic HEI gives rise a radial force along $\hat{\boldsymbol{r}}_{ij}$ in terms of $\boldsymbol{\varphi}_{ij} = \hat{\boldsymbol{r}}_{ij}(\boldsymbol{S}_i \cdot \boldsymbol{S}_j)$. Further, the DMI will lead to an additional tangential force component associated with $\boldsymbol{A}_{ij}^{\perp}$, which determines the feature of lattice microstructure.

In the following, we will consider various specific spin textures $\{\boldsymbol{S}_i\}$ upon a given crystal structure to analyze the atomic force of an arbitrary atom $\boldsymbol{f}_i$ provided by its neighbors, and then to obtain the equilibrium lattice configuration $\{\boldsymbol{r}_i\}$ under the condition of $\boldsymbol{f}_i = 0$.

B. The expression of interatomic force for a given skyrmion spin texture

For clarity and without loss of generality, we consider a single skyrmion spin texture on a surface and the resulting LLDF. Plotted in Fig. 2(a), we set the position of skyrmion center as the origin. In this case, the spin $\boldsymbol{S}_i = \boldsymbol{S}(\boldsymbol{r}_i)$ located at $\boldsymbol{r}_i$ from the skyrmion core can be parameterized in a three dimensional (3D) ball as [29]

$$\boldsymbol{S}(\boldsymbol{r}_i) = \text{sign}(Q)(\sin\Theta_i\cos\Phi_i, \sin\Theta_i\sin\Phi_i, \cos\Theta_i), \tag{7}$$

where $\boldsymbol{r}_i = r_i\cos\phi_i\hat{x} + r_i\sin\phi_i\hat{y}$ with $r_i = |\boldsymbol{r}_i|$ and ϕ_i as the polar angle on the surface. $Q = \pm 1$ is the topological charge of a single skyrmion. Φ_i and Θ_i are the polar and azimuthal angles in the 3D ball, respectively, associated with ϕ_i and r_i as $\Phi_i = \phi_i + Q_h$ and $\cos\Theta_i = (r_i - \lambda)/(r_i + \lambda)$. Q_h is the helicity number. $Q_h = 0$ or π and $Q_h = \pm\pi/2$ are respectively for the Néel and Bloch skyrmions. λ is the skyrmion size.

For the skyrmion state, substituting the spin configuration $\boldsymbol{S}_i = \boldsymbol{S}(\boldsymbol{r}_i)$ of Eq. (7) into the terms of $\boldsymbol{A}_{ij}$ associated with the

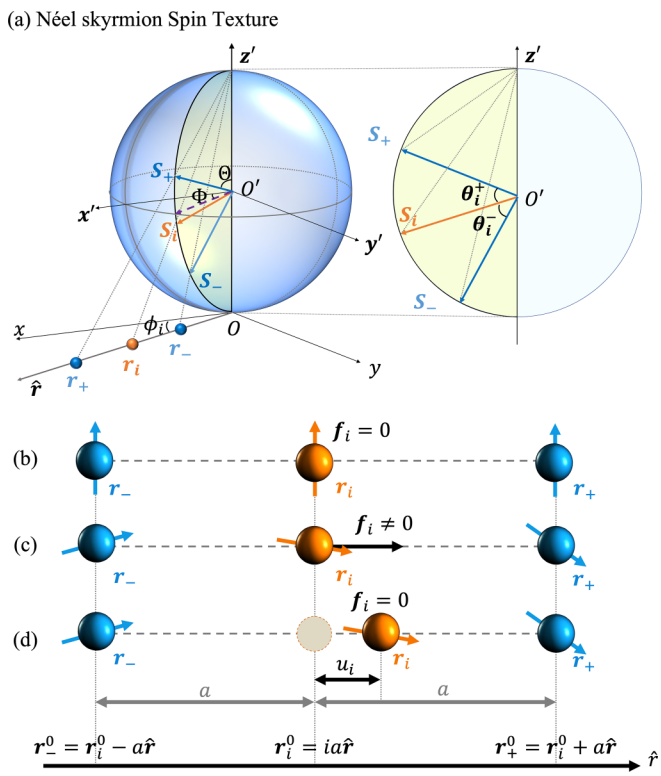

FIG. 2. The diagram of three aligned atoms with spins ($\boldsymbol{S}_-$, $\boldsymbol{S}_i$, and $\boldsymbol{S}_+$,) attached on them located at different sites ($\boldsymbol{r}_-$, $\boldsymbol{r}_i$, and $\boldsymbol{r}_+$,). The change of the spin orientation, accompanied by the adjustment of interactions among atoms, results in a deviation u_i of the spin location.

corresponding type of DMI, we have (see detail within the Supplemental Material [30])

$$\begin{aligned} \boldsymbol{A}^{\parallel}_{i,\pm} &= \pm \sin\theta^{\pm}_i \hat{\boldsymbol{r}} && \text{radical component,} \\ \boldsymbol{A}^{\perp}_{i,\pm} &= 0 && \text{tangential component} \end{aligned} \tag{8}$$

where $\boldsymbol{A}_{i,\pm} \equiv \boldsymbol{A}_{ij}$ with j being the left and right neighboring atoms of the ith atom along the given direction of $\hat{r}$, denoted by $j = i \pm 1$, and $\theta^+_i = \Theta_i - \Theta_+$ and $\theta^-_i = \Theta_- - \Theta_i$ shown in Fig. 2(a), representing the azimuthal angle between the adjacent spin vector. Therefore, Eq. (8) indicates the fact, that no matter the skyrmion spin texture is of Bloch- or Néel-type, we can always have the conclusion that noncollinear spin alignment does not give rise to the tangential force. In this regard, we can update the expression of interatomic force $\boldsymbol{f}_{ij}$ upon the given spin texture of skyrmion described by Eq. (7) as

$$\boldsymbol{f}_{ij} = -U'(r_{ij})\hat{r}_{ij} + J'(r_{ij})\boldsymbol{\varphi}_{ij} + D'(r_{ij})\boldsymbol{A}^{\parallel}_{ij} \equiv f_{ij}\hat{r}_{ij}, \tag{9}$$

where there is only the radial component along $\hat{r}_{ij}$. Here, $X'(r_{ij}) \equiv \frac{\partial X}{\partial r_{ij}}$ with $X = U, J, D$.

C. The force analysis

Let us now consider the total force $\boldsymbol{f}_i$ exerted by an ith atom, which is provided by its neighboring atoms, i.e., $\boldsymbol{f}_i = \sum_{j\in NN} \boldsymbol{f}_{ij}$. Here, we can consider a simplest case as shown in Fig. 2, where there are three adjacent spins (i.e., $\boldsymbol{S}_i$ and $\boldsymbol{S}_\pm$) at their lattice sites (i.e., $\boldsymbol{r}_i$ and $\boldsymbol{r}_\pm$) along a crystalline direction $\hat{r}$, and $\boldsymbol{r}_i = ia\hat{r}$ and $\boldsymbol{r}_\pm = \mp\hat{r}$, with a as the lattice parameter along the $\hat{r}$ direction.

Figures 2(b)–2(d) qualitatively show the effects of spin texture to the interatomic force and the resulting lattice configuration. Note that, in the case of $\boldsymbol{A}_{ij} = 0$ for a spin configuration at the ferromagnetic (FM) phase, the lattice subsystem will keep stable at a regular lattice configuration denoted by $\{\boldsymbol{r}^0_i\}$, as shown in Fig. 2(b). Otherwise, in the case of $\boldsymbol{A}_{ij} \neq 0$ at a skyrmion phase, we can get $\boldsymbol{A}_{ij} \neq \boldsymbol{A}_{ji}$ due to the broken inversion symmetry described by the DMI, so that $\boldsymbol{f}_i \neq 0$ for an arbitrary i atom apart from the skyrmion center. In other words, $\boldsymbol{r}^0_i$ is no longer its stable position owed to the asymmetric interaction induced by the SLC (including the DMI and the spiral spin configuration).

On the other hand, the quantitative description of $\boldsymbol{f}_i$ for the structure shown in Fig. 2(c) can be obtained by following Eq. (9), as

$$\begin{aligned} \boldsymbol{f}_i &= \boldsymbol{f}_{i,-} + \boldsymbol{f}_{i,+} \\ &= (-\hat{r}_{i,-}U'(r_{i,-}) - \hat{r}_{i,+}U'(r_{i,+})) \\ &\quad + (\boldsymbol{\varphi}_{i,-}J'(r_{i,-}) + \boldsymbol{\varphi}_{i,+}J'(r_{i,+})) \\ &\quad + (\boldsymbol{A}^{\parallel}_{i,-}D'(r_{i,-}) + \boldsymbol{A}^{\parallel}_{i,-}D'(r_{i,-})) \\ &\equiv \boldsymbol{f}^L_i + \boldsymbol{f}^J_i + \boldsymbol{f}^D_i. \end{aligned} \tag{10}$$

Here, for the first right-hand side terms $\boldsymbol{f}^L_i$ of Eq. (10), we can get

$$\begin{aligned} \boldsymbol{f}^L_i &= -\hat{r}_{i,-}U'(r_{i,-}) - \hat{r}_{i,+}U'(r_{i,+}) \\ &= -\hat{r}(U'(r_{i,-}) - U'(r_{i,+})) = 0, \end{aligned} \tag{11}$$

because $U'(r_{i,-}) = U'(r_{i,+}) = U'(a)$ as $r_{i,-} = r_{i,+} = a$. For the second right-hand side terms $\boldsymbol{f}^J_i$ of Eq. (10), we can get

$$\begin{aligned} \boldsymbol{f}^J_i &= \boldsymbol{\varphi}_{i,-}J'(r_{i,-}) + \boldsymbol{\varphi}_{i,+}J'(r_{i,+}) \\ &= \hat{r}J'(a)(\cos\theta^-_i - \cos\theta^+_i) = J'(a)G^-_i\hat{r}, \end{aligned} \tag{12}$$

where we use $J'(r_{i,-}) = J'(r_{i,+}) = J'(a)$ due to $r_{i,-} = r_{i,+} = a$ and $\boldsymbol{\varphi}_{i,\pm} = \mp\cos\theta^{\pm}_i\hat{r}$, and $G^-_i = \cos\theta^-_i - \cos\theta^+_i$. For the third right-hand side terms $\boldsymbol{f}^D_i$ of Eq. (10), we can get

$$\begin{aligned} \boldsymbol{f}^D_i &= \boldsymbol{A}^{\parallel}_{i,-}D'(r_{i,-}) + \boldsymbol{A}^{\parallel}_{i,-}D'(r_{i,-}) \\ &= \hat{r}D'(a)(\sin\theta^+_i - \sin\theta^-_i) = D'(a)K^-_i\hat{r}, \end{aligned} \tag{13}$$

where we use $D'(r_{i,-}) = D'(r_{i,+}) = D'(a)$ due to $r_{i,-} = r_{i,+} = a$ and $\boldsymbol{A}_{i,\pm} = \pm\sin\theta^{\pm}_i\hat{r}$ and $\boldsymbol{A}^{\perp}_{i,\pm} = 0$, and $K^-_i = \sin\theta^+_i - \sin\theta^-_i$. Therefore,

$$\boldsymbol{f}_i = (J'(a)G^-_i + D'(a)K^-_i)\hat{r} = f_i\hat{r}, \tag{14}$$

which is a radial force. Since Θ_i is the function of r_i and λ, G_i, and K_i can also be written as $G^-_i(r_i, \lambda)$ and $K^-_i(r_i, \lambda)$. For a given skyrmion spin texture, $G^-_i < 0$ and $K^-_i < 0$ always hold, because $\Theta_{i-1} > \Theta_i > \Theta_{i+1}$ and $\theta^-_i > \theta^+_i > 0$. In addition, $J(r_{ij})$ is determined by the electronic wave function overlap of the ith and jth atoms, which is thus a decrease function of r_{ij}, so that $J'(a) < 0$ [15]. Meanwhile, $D(r_{ij})$ is also found to negatively rely on r_{ij} [31], thus $D'(a) < 0$. According to Eq. (14), $f_i > 0$, and $\boldsymbol{f}_i$ will point to the crystalline direction $\hat{r}$, leading to the lattice relaxation away from the

skyrmion core for an arbitrary ith atom. Note that, in Fig. 2, the radial neighboring atoms provide the radial force to the ith atom. In fact, the tangential neighboring atoms also give only the radial force (see detailed deduction in the Supplemental Material [30]). In this regard, based on either Block- or Néel-type skyrmion, there is no tangential force exerted by any arbitrary atom.

To sum up, given a skyrmion spin texture, an arbitrary atom stays at its regular site apart from skyrmion core will exert an radial force, so that it will relax to the new equilibrium position apart from its regular site to make $\boldsymbol{f}_i = 0$, which is illustrated in Fig. 2(d). Therefore, an LLDF can be observed for a given skyrmion spin texture as schematics as in Fig. 1. In the following, we will get the LLDF morphology of a skyrmion by the force analysis.

D. The microdynamic morphology of LLDF

As shown in Fig. 2(d), assume that the positions of $(i \pm 1)$th spins are fixed, and the ith spin moves to $\boldsymbol{r}_i = \boldsymbol{r}_i^0 + u_i\hat{\boldsymbol{r}}$, so to make $\boldsymbol{f}_i = 0$. We can now define the lattice distortion ε_i of ith atom as

$$\boldsymbol{\varepsilon}(\boldsymbol{r}_i) = \varepsilon_i\hat{r} = \left(\boldsymbol{r}_i - \boldsymbol{r}_i^0\right)/a = \hat{r}(u_i/a), \tag{15}$$

so that $\boldsymbol{\varepsilon}(\boldsymbol{r}_i) = \varepsilon_i\hat{r}$ is exactly the LLDF considered in this paper. Referring to Eq. (10), there are three parts in $\boldsymbol{f}_i$ while $\boldsymbol{r}_i = \boldsymbol{r}_i^0 + u_i\hat{r}$, i.e., $\boldsymbol{f}_i = \boldsymbol{f}_i^L + \boldsymbol{f}_i^J + \boldsymbol{f}_i^D$. For $\boldsymbol{f}_i^L$, we have

$$\boldsymbol{f}_i^L = \boldsymbol{f}_{i,i-1}^L + \boldsymbol{f}_{i,i+1}^L = [U'(a+u_i) - U'(a-u_i)]\hat{r}. \tag{16}$$

Suppose $|u_i| \ll a$, and $U(r_{ij})$ can be expanded harmonically at $r_{ij} = a$ as

$$U(r_{ij}) = U(a) + \frac{1}{2}U''(a)u_i^2 = U(a) + \frac{1}{2}B\Omega\frac{u_i^2}{a^2} \tag{17}$$

where B is the bulk modulus and Ω is the atomic volume. Therefore, we can get

$$\boldsymbol{f}_i^L = 2u_iU''(a)\hat{r} = \frac{2B\Omega}{a}\varepsilon_i\hat{r}. \tag{18}$$

The part of $\boldsymbol{f}_i^J$ can be derived as

$$\begin{aligned}\boldsymbol{f}_i^J &= \boldsymbol{f}_{i,i-1}^J + \boldsymbol{f}_{i,i+1}^J \\ &= [J'(a-u_i)\cos\theta_i^- - J'(a+u_i)\cos\theta_i^+]\hat{r}.\end{aligned} \tag{19}$$

In the limit of $|u_i| \ll a$, we can get

$$J'(a \pm u_i) \approxeq J'(a) \pm u_iJ''(a), \tag{20}$$

so that

$$\boldsymbol{f}_i^J = [J'(a)G_i^-(\lambda) - u_iJ''(a)G_i^+(\lambda)]\hat{r} \tag{21}$$

with $G_i^+(\lambda) = \cos\theta_i^- + \cos\theta_i^+$. Furthermore, since the ferromagnetic background state of the magnetic system we considered, the HEI strength $J(a)$ has positive value. Because $J(r_{ij})$ usually shows the negative dependence with the increasing atomic distance r_{ij} [15], we can conclude that

$$J'(a) \sim -J(a)/a, \text{ and } J''(a) \sim J(a)/a^2. \tag{22}$$

Finally we can get

$$\boldsymbol{f}_i^J = -\frac{J(a)}{a}[G_i^-(\lambda) + \varepsilon_iG_i^+(\lambda)]\hat{r}, \tag{23}$$

where all the complicated r_i dependence of $J'(a)$ and $J''(a)$ is absorbed into the undetermined coefficients of $G_i^-(\lambda)$ and $G_i^+(\lambda)$.

Similarly, we can rewrite $\boldsymbol{f}_i^D$ in the same way as

$$\boldsymbol{f}_i^D = -\frac{D(a)}{a}[K_i^-(\lambda) + \varepsilon_iK_i^+(\lambda)]\hat{r} \tag{24}$$

with $K_i^+(\lambda) = \sin\theta_i^+ + \sin\theta_i^-$. Note that the HEI strength $J(a)$ is associated with the Curie temperature T_C for the ferromagnetic and paramagnetic phase transition [42], as $J(a) \sim 2k_BT_C$, and $D(r_{ij})$ is usually assumed to have a similar r_{ij} dependence with that of $J(r_{ij})$ [20]. Therefore, $\boldsymbol{f}_i^J$ and $\boldsymbol{f}_i^D$ can combine together, and be written in term of

$$\begin{aligned}\boldsymbol{f}_i^J + \boldsymbol{f}_i^D &= -\frac{J(a)}{a}[G_i^-(\lambda) + \varepsilon_iG_i^+(\lambda)]\hat{r} \\ &\quad - \frac{D(a)}{a}[K_i^-(\lambda) + \varepsilon_iK_i^+(\lambda)]\hat{r} \\ &= -\frac{J(a)}{a}[G_i^-(\lambda) + bK_i^-(\lambda)]\hat{r} \\ &\quad - \frac{J(a)}{a}\varepsilon_i[G_i^+(\lambda) + bK_i^+(\lambda)]\hat{r} \\ &= -\frac{2k_BT_C}{a}\left[\frac{1}{h_i(\lambda)} - \varepsilon_i\frac{g_i(\lambda)}{h_i(\lambda)}\right]\hat{r}.\end{aligned} \tag{25}$$

Here, we simply set $D = bJ$, with b as the D/J ratio. We further define

$$\begin{aligned}\frac{1}{h_i(\lambda)} &\equiv +[G_i^-(\lambda) + bK_i^-(\lambda)] \\ \frac{g_i(\lambda)}{h_i(\lambda)} &\equiv -[G_i^+(\lambda) + bK_i^+(\lambda)]\end{aligned}$$

to describe the actions related to the detail of spin texture and the r_{ij} dependence of the magnetic HEI and DMI.

In this regard, when the ith atom stays at the position of $\boldsymbol{r}_i = \boldsymbol{r}_i^0 + a\varepsilon_i\hat{r}$, the atomic force $\boldsymbol{f}_i$ is null, i.e.,

$$\boldsymbol{f}_i = \left(\frac{2B\Omega}{a}\varepsilon_i - \frac{2k_BT_C}{a}\left[\frac{1}{h_i(\lambda)} - \varepsilon_i\frac{g_i(\lambda)}{h_i(\lambda)}\right]\right)\hat{r} = 0. \tag{26}$$

We can then achieve the analytical expression of ε_i as

$$\varepsilon_i = \frac{k_BT_C}{g_i(\lambda)k_BT_C + h_i(\lambda)B\Omega} \equiv \frac{\eta}{g_i(\lambda)\eta + h_i(\lambda)}, \tag{27}$$

where $\eta = k_BT_C/B\Omega$ is defined to characterize the competition between the magnetic and mechanical interactions. The resultant $\boldsymbol{f}_i$ and ε_i reflect the physical essence of effects from the skyrmion spin texture and the intrinsic SLC involved. For instance, the undetermined coefficients of g_i and h_i as functions of skyrmion size λ are morphology of skyrmion spin texture, and the defined η naturally implies the actions of SLC.

E. Numerical simulation of LLDF

In the following, the numerical simulations based on spin-lattice dynamics (SLD) are performed to check the validity of Eq. (27) for the LLDF of ε_i. SLD is an atomistic method that provides a real-time description of spin-lattice coupling in magnetic materials. In the numeric simulation of LLDF, the spin texture is preset as either Block- or Néel-type skyrmion,

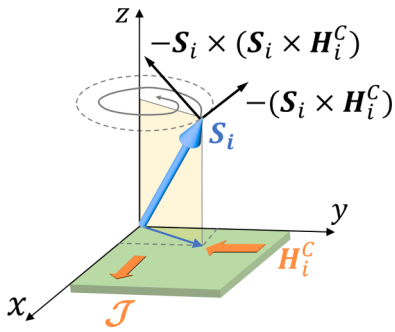

FIG. 3. The actions on an atomic spin provided by the applied current $\mathcal{J}$: the field-like torque $-(\boldsymbol{S}_i \times \boldsymbol{H}_i^C)$ and the damped-like torque $-\boldsymbol{S}_i \times (\boldsymbol{S}_i \times \boldsymbol{H}_i^C)$. Here, $\boldsymbol{H}_i^C$ is the effective magnetic field associated with $\mathcal{J}$ as written as in Eq. (30).

and the lattice configuration is relaxed to make $\boldsymbol{f}_i = 0$ for any atoms.

In SLD, the coupled spin and lattice dynamics are described by a Langevin equation, derived from the Hamiltonian of Eq. (1), as

$$\begin{aligned}
\dot{\boldsymbol{r}}_i &= \boldsymbol{p}_i/m \\
\dot{\boldsymbol{p}}_i &= -\frac{\partial U}{\partial \boldsymbol{r}_i} + \sum_j{}' \left[\frac{\partial J}{\partial r_{ij}} \boldsymbol{\varphi}_{ij} + \frac{\partial D}{\partial r_{ij}} \boldsymbol{A}_{ij}^{\parallel} + \frac{D}{r_{ij}} \boldsymbol{A}_{ij}^{\perp} \right] \\
&\quad - \gamma_L \boldsymbol{p}_i + \boldsymbol{\xi}_i(t) \\
\hbar \dot{\boldsymbol{S}}_i &= \boldsymbol{S}_i \times [\boldsymbol{H}_i + \boldsymbol{h}_i(t)] - \gamma_i^S \boldsymbol{S}_i \times (\boldsymbol{S}_i \times \boldsymbol{H}_i) \\
&\quad - \gamma_S c_{\parallel} \boldsymbol{S}_i \times \left(\boldsymbol{S}_i \times \boldsymbol{H}_i^C\right) - \gamma_S c_{\perp} \boldsymbol{S}_i \times \boldsymbol{H}_i^C .
\end{aligned} \tag{28}$$

Here, $\boldsymbol{H}_i$ is the intrinsic effective field of the ith spin, expressed as

$$\boldsymbol{H}_i = \sum_j{}' [J(\boldsymbol{r}_{ij}) \boldsymbol{S}_j + \boldsymbol{S}_j \times \boldsymbol{D}(\boldsymbol{r}_{ij}) + \boldsymbol{H}_{\text{ext}}]. \tag{29}$$

$\boldsymbol{H}_i^C$ is the effective field induced by the electric current $\mathcal{J}$ applied, as [see Fig. 3 to check the actions of current on spin described in Eqs. (28)]

$$\boldsymbol{H}_i^C = \frac{\hbar \theta_{SH}}{2eS} \mathcal{J} \times \hat{z}, \tag{30}$$

where $\hbar$ is the Planck's constant, $e = 1.602 \times 10^{-19}$ C is the electronic charge, $S = 1$ is the magnitude of atomic spin $\boldsymbol{S}_i$, $\theta_{SH} = 0.12$ is the spin Hall angle, and $\hat{z}$ is the normal vector of the thin film or interface having the skyrmion spin texture. $c_{\parallel}$ and $c_{\perp}$ are the coefficients of the field induced by external current $\mathcal{J}$ applied. Here, we choose $c_{\parallel} = 1$, and $c_{\perp} = 0.1 c_{\parallel}$ [43]. In Eqs. (28), the spin-lattice coupling is included in $J(\boldsymbol{r}_{ij})$ and $\boldsymbol{D}(\boldsymbol{r}_{ij})$, both of which are the functions of $\boldsymbol{r}_{ij}$. γ_L and γ_S are the friction coefficients of lattice and spin dynamics. $\boldsymbol{\xi}_i(t)$ and $\boldsymbol{h}_i(t)$ in Eq. (28) are the Gaussian-type random force for lattice dynamics and random field for the spin dynamics, respectively. According to the fluctuation-dissipation theorem [16], we have

$$\begin{aligned}
\langle \xi_{i\alpha}(t) \rangle &= 0 \\
\langle \xi_{i\alpha}(t) \xi_{j\beta}(t') \rangle &= 2\gamma_L k_B T \delta_{ij} \delta_{\alpha\beta} \delta(t - t') \\
\langle h_{i\alpha}(t) \rangle &= 0 \\
\langle h_{i\alpha}(t) h_{j\beta}(t') \rangle &= 2\gamma_S k_B T \delta_{ij} \delta_{\alpha\beta} \delta(t - t').
\end{aligned} \tag{31}$$

By solving Eqs. (28), the trajectory and the momentum of skyrmion are obtained.

Bloch skyrmion and Néel skyrmion are generally found in chiral magnets and ferromagnetic/heavy metal such as MnGe [44] and Fe/Ir(111) [45] with simple-cubic structure. The lattice constant of MnGe is $a = 4.79$ Å and for Fe/Ir(111) is $a = 3.84$ Å. Accordingly, $J_{ij}(\boldsymbol{r}_{ij})$ and $D_{ij}(\boldsymbol{r}_{ij})$ vary with different materials. Here, we adopt the same forms of $J_{ij}(\boldsymbol{r}_{ij})$ and $D_{ij}(\boldsymbol{r}_{ij})$ as Ref. [17]

$$\begin{aligned}
J(\boldsymbol{r}_{ij}) &= J(r_{ij}) = J_0 \cdot (1 - r_{ij}/r_c)^3 \\
D(\boldsymbol{r}_{ij}) &= [bJ(\boldsymbol{r}_{ij})] = b \cdot J_0 \cdot (1 - r_{ij}/r_c)^3,
\end{aligned} \tag{32}$$

where b is the so-called D/J ratio, and it determines the skyrmion size. Here, $b = 0.31$ for Fe/Ir(111), and $b = 0.13$ for MnGe. J_0 and r_c are fitted from the lattice parameter and the Curie temperature. Here, $J_0 = 64.15$ meV. $r_c = 7.124$ Å for Fe/Ir(111) and $r_c = 8.935$ Å for MnGe. As discussed in Ref. [17], the r_{ij} dependence of J and D determine the detailed LLDF morphology, but will not bring any significant influence of the qualitative discussion about the microdynamic feature of LLDF and its effects on skyrmion transport and stability. To avoid the surface effect, an isotropic box with size of 60×100 with period boundary condition is applied in the simulation. The phase trajectories are solved by the integration algorithm based on the concept of Suzuki-Trotter decomposition [46] with parallel programming implementation [47].

An illustrative diagram of LLDF is plotted in Fig. 4(a), which guides the simulation results. The first layer of it represents the Néel skyrmion spin texture and the third layer depicts the LLDF induced by this skyrmion. To get intuitive description to the magnitude of LLDF, the second layer is inserted, in which the distance from the skyrmion center is marked as r. In the second layer of the sandwich structure, the degree of surface undulation is determined by the strength of LLDF ε_i. Figure 4(a) also shows that ε_i reaches its peak $\varepsilon_{\max} = \max\{\varepsilon_i\}$ at the central position of the skyrmion. Therefore, We use the maximum strain $\varepsilon_{\max}$ to denote the strength and the gradient $\varepsilon_i' = \frac{\partial \varepsilon_i}{\partial r_i}$ to denote the spatial range, both of which is used to characterize the morphology of LLDF.

A nonlinear intrinsic strain field of the resulting LLDF is shown in Fig. 4(b), where $\varepsilon_{\max} \sim 20 \times 10^{-3}$ and a negative strain gradient rapidly reduces from $3 \times 10^{-3}/\lambda$ to $2 \times 10^{-3}/\lambda$ within one skyrmion size, and vanishes in a triple skyrmion size. In addition, given a skyrmion size λ, the strength of strain field denoted by $\varepsilon_{\max}$ has the same η-dependence with that of Eq. (27), independent of the type of DMI or spin texture, which is confirmed by simulation data plotted in Fig. 4(c), that increasing the magnetoelastic coupling strength as rising up η will lead to a stronger LLDF. Here, we choose $\lambda = 15$ Å and 5 Å, which are respectively the skyrmion sizes of MnGe and Fe/Ir as the prototypes of the Bloch and Néel skyrmions. On the other hand, given

TABLE I. Parameters determining the morphology of LLDF in some selective chiral magnets.

Material	Skyrmion type	Ω [Å^3]	B [GPa]	T_C [K]	λ[a] [Å]	η [$\times 10^{-3}$]	$\varepsilon_{\max}$ [$\times 10^{-3}$]
MnSi	Bloch	94.07 [1]	167.00 [33]	28.50 [1]	90	0.025	0.184
MnGe	Bloch	106.70 [34]	88.01 [33]	187.00 [35]	15–30	0.275	9.518
FeGe	Bloch	105.97 [36]	162.98 [37]	279.10 [38]	350	0.223	0.413
Fe/Ir(111)	Néel	55.03 [39]	277.83 [40]	300.00 [41]	5	0.271	19.674

[a]Data are obtained from Ref. [32], where the diameter is considered as skyrmion size, and twice of λ used in here.

the magnetoelastic coupling strength η (i.e., $\eta = 10^{-3}$ for MnGe and $\eta = 10^{-3}$ for Fe/Ir), a smaller skyrmion leads to a more twisted spin spirality, thus a stronger LLDF. Hence, $\varepsilon_{\max}$ reduces rapidly with increasing λ as shown in Fig. 4(d). Experimentally, the smallest skyrmion hosted in the Fe/Ir with radius of $\lambda = 5$ Å, while the upper limit of skyrmion size can reach hundreds of nanometers. Therefore, the LLDF of a skyrmion can reach a maximum of 2×10^{-3} and decrease to 0 asymptotically with increasing skyrmion size [32]. To

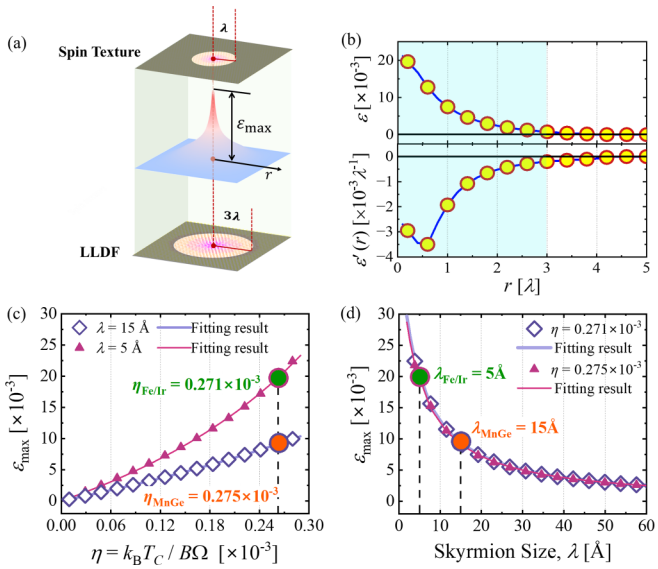

FIG. 4. (a) The relationship of Néel skyrmion spin texture and the irrotational LLDF. An isolated skyrmion being hosted in a lattice can be treated as a sandwich structure. The first layer of it represents the Néel skyrmion spin texture and the third layer depicts the LLDF induced by this skyrmion. To get intuitive description to the magnitude of LLDF, the second layer is inserted, in which the distance from the skyrmion center is marked as r. In the second layer of the sandwich structure, the degree of surface undulation is determined by the strength of LLDF. Therefore, at the central position of the skyrmion, LLDF reaches its peak $\varepsilon_{\max}$. (b) The morphology of LLDF induced by skyrmion spin texture in Fe/Ir. The strength of LLDF ε reduces rapidly as increasing atomic distance r, resulting in a negative strain gradient ε_i'. (c) To represent the modulating effect of B and T_C on the LLDF strength denoted by $\varepsilon_{\max}$, as function of $\eta = k_B T_C / B\Omega$. $\varepsilon_{\max}$ rises with growing η but declines as the skyrmion size λ increases. (d) The relation of the LLDF strength denoted by $\varepsilon_{\max}$ against λ with $\eta = 10^{-3}$ and 10^{-3}, respectively. In both (c) and (d), the magenta-colored and the violet lines represent the fitting results in two different cases based on Eq. (27) and the fitting parameters are provided in Table I.

get closer observation of the LLDF morphology, we take Fe/Ir as an example and display its corresponding LLDF in Fig. 5. It shows that the growth of η is accompanied with the increasing $\varepsilon_{\max}$. Cases (1), (2), and (3) are the snapshots of LLDF when $\eta = 10^{-3}$, 10^{-3}, and 10^{-3} in a given simulation box having 344 skyrmion size of $\lambda = 5$ Å. Similarly, Fig. 5 illustrates that increasing the skyrmion size λ leads to the drop of the strength of LLDF denoted by $\varepsilon_{\max}$. Cases (4), (5), and (6) are the snapshots of LLDF when $\lambda = 5$ Å, 15 Å, and 35 Å with fixed η which is set to be 10^{-3}. Therefore, Fig. 5 can also reclaim the conclusion we obtained in Fig. 4.

From the discussion above, it can be confirmed that LLDF represents a nonlinear local strain field, arising inevitably from the intrinsic SLC within a spiral spin texture background in skyrmion materials, as described in Eq. (27). The strength of the SLC is governed by the magnetomechanical coupling parameter η and the spiral spin texture denoted by the skyrmion size λ. Equation (27) also reveals that the LLDF can be predicted if bulk modulus B and Curie temperature T_C are known. Table I lists the parameters of B, T_C, and λ for some selective chiral magnetic materials or systems, as well as the corresponding $\varepsilon_{\max}$ of LLDF. Interestingly, the morphology of the LLDF is independent of the topological feature of skyrmion spin texture. It can be seen in the expression of the atomic force $\boldsymbol{f}_i$ in Eq. (14) or the strain field ε_i in Eq. (27), the LLDF morphology is mainly determined by the skyrmion size λ, and independent with the chirality characterized by the topological charge Q and the helicity number Q_h. Therefore, reversing the skyrmion chirality cannot significantly change the divergence nature of the LLDF. On the other hand, the spin-lattice coupling nature is another factor that determines the LLDF morphology. If one can get a positive r_{ij} dependence of the magnetic interaction strengths, like HEI $J' > 0$ or DMI $D' > 0$, the resulting LLDF will reveal an irrotational field with drain. Furthermore, both magnetic and mechanical properties, as well as the skyrmion size, are sensitive to the magnetic or mechanical loading [48,49], so that the LLDF will be easily modulated [33–39,41,44]. Finally, the magnitude of the intrinsic LLDF is a small nonlinear strain field compared to the one as the response to an applied external mechanical stress. It is not easy to be observed by experiment. In particular, to obtain the direct observation of LLDF requires the high-resolution spatial experimental instrument at low temperatures, like transmission electron microscope (TEM). Fortunately, it brings with significant dynamic and thermodynamic effects on the evolution of skyrmion spin texture, which will be discussed in the following section.

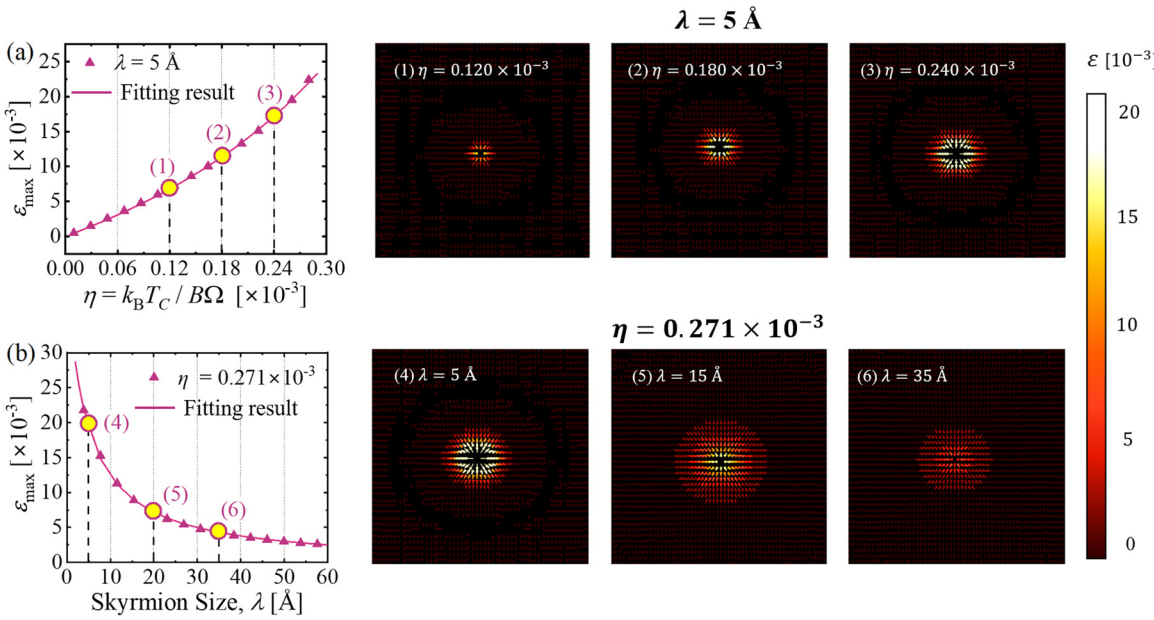

FIG. 5. (a) Taking the Fe/Ir case in Fig. 4 as an example, the illustration of LLDF in Fe/Ir when (1) $\eta = 10^{-3}$, (2) $\eta = 10^{-3}$, and (3) $\eta = 10^{-3}$ with $\lambda = 5$ Å. The size of LLDF expands as η increases. (b) The snapshots of LLDF when (4) $\lambda = 5$ Å, (5) $\lambda = 15$ Å, and (6) $\lambda = 35$ Å with $\eta = 10^{-3}$. The size of LLDF shrinks as λ increasing. The magenta-colored lines in both (a) and (b) represent the fitting result of the LLDF in Fe/Ir according to Eq. (27).

III. EFFECTS OF LLDF ON THE TRANSPORT AND STABILITY OF SKYRMION

In this section, we delve into the discourse concerning the influence of LLDF on skyrmion transport and stability. It is known that the size of skyrmion is a reflection of the magnitude of SLC. Since the LLDF is naturally accompanied by the skyrmion, so that the size of skyrmion is corresponding to the strength of LLDF. To be more precise, a reduction in the skyrmion size signifies an augmentation of the SLC, leading to a heightened LLDF effect, thus hindering the skyrmion motion and devastating the stability of skyrmion.

According to statistical thermodynamics, the transport of skyrmion at finite temperature can be regarded as the Brownian motion upon a potential surface $U(X)$. A generalized Langevin equation [50] can describe the dynamical evolution behavior as

$$m\ddot{X} = -\partial U/\partial X - \gamma \dot{X} + \xi(t). \tag{33}$$

Here X is the generalized coordinate denoting the state that the skyrmion system stays in. Setting X as the skyrmion center position r_S in the real space converts Eq. (33) into the Thiele equation [51] describing the transport behavior as plotted in Fig. 6(a). Correspondingly, Eq. (33) describes the creation or annihilation of skyrmion spin texture by setting X as the topological charges Q as the generalized coordinate in the phase space as plotted in Fig. 6(a). For instance, the system moving from $Q = 1$ to 0 denotes the annihilation of a single skyrmion spin texture to the ferromagnetic (FM) state. m is the corresponding effective mass. γ is the friction coefficient and $\xi(t)$ is the random force, both of which are arising from the heat bath. U is the conservative potential modified by an external field applied, owed to either a periodic potential exerted by LLDF in transport [18] or the energy required to break down its topological protection in microstructural evolution [50]. Note that the generalized Langevin equation proposed here is to provide an intuitive physical picture of the spin-texture transport and phase transition. In the following, we will directly perform the SLD simulations to discuss the effects of LLDF.

A. Effect of LLDF on skyrmion transport

In the following, we will analyze such LLDF effects on the skyrmion transport by performing SLD simulations for an isotropic and defect-free Fe/Ir thin film, with LLDF where the SLC is involved (denoted by $\mathcal{H}_{S+L}$), and without LLDF, which only includes spin dynamics upon a regular lattice configuration (denoted by $\mathcal{H}_S$). Firstly, a single skyrmion with size of λ will be generated under a given temperature and external magnetic field applied for a stress-free system of Fe/Ir. Subsequently, the isothermal-isobaric ensemble is applied to perform the simulation of current-induced motion of skyrmion. The current density $\mathcal{J} = I/A$ is set to be 2.23, 34.3, and 103 in the unit of 10^8 A/m^2, respectively. Here, I is the electric current and A is the area of the material.

In the system of $\mathcal{H}_S$, the skyrmion spin texture can be driven by the applied external force (i.e., the electric current $\mathcal{J}$ used in this paper), whose drifted velocity linearly depends on the external force strength as plotted in Figs. 6(b)–6(d). However, as well addressed in Ref. [17], the presence of LLDF gives rise to an energy barrier E_m, so to drag the transport of spin texture, which is as schematic in Fig. 6(a). In brief, the nonlinear skyrmion transport behavior is arising from the dragging force with periodic spatial distribution, most possibly provided by the LLDF, not lattice defects. In our

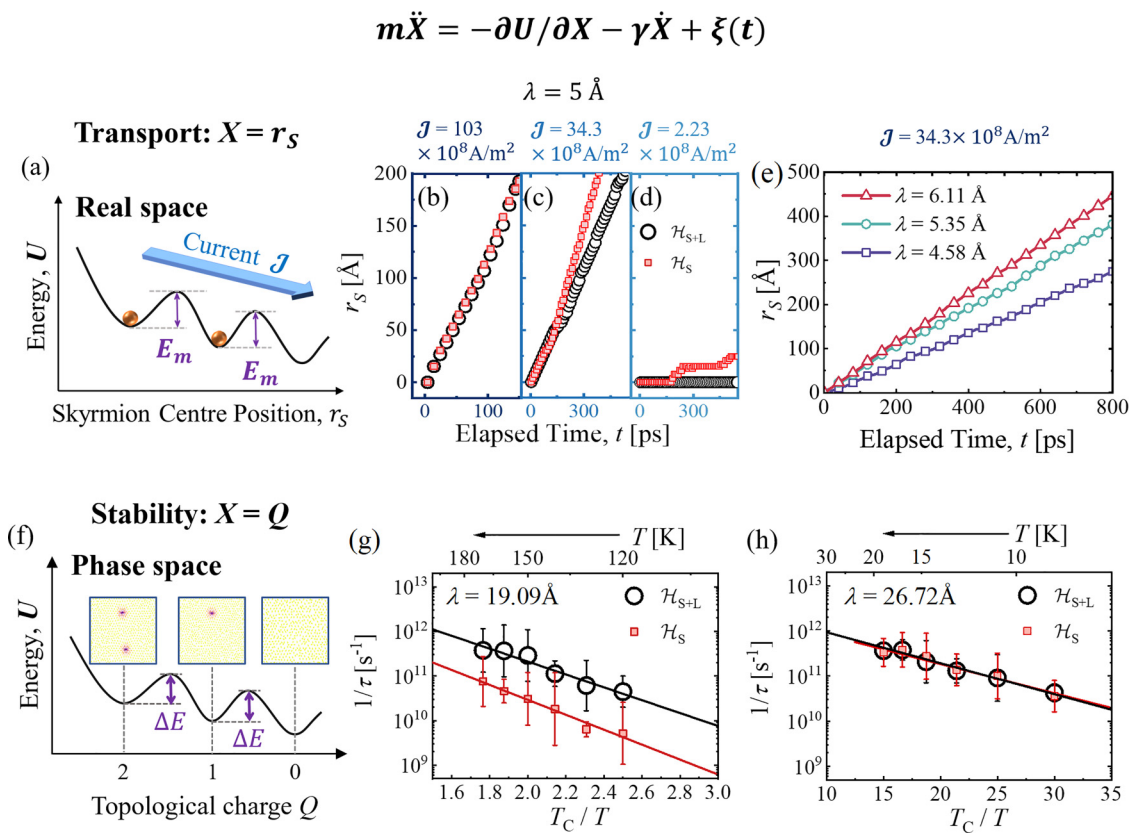

FIG. 6. The influence of LLDF on skyrmion motion and stability. (a) Schematic of skyrmion transport with LLDF in real-space under a current $\mathcal{J}$ applied, where the energy barrier E_m is owed to the dragging effects of LLDF. The time-dependence of skyrmion center motion under various $\mathcal{J}$ is represented as the skyrmion trajectory. Here, the current with strengths of (b) $\mathcal{J} = 103$, (c) $\mathcal{J} = 34.3$ and (d) $\mathcal{J} = 2.23$ in the unit of 10^8 A/m^2 are applied. (e) Skyrmion trajectories $r_S(t)$ in $\mathcal{H}_{S+L}$ with various sizes as $\lambda = 4.58$ Å (the purple squares), $\lambda = 5.35$ Å (the green circles) and $\lambda = 6.11$ Å (the red triangles) under a given $\mathcal{J} = 34.3 \times 10^8$ A/m^2. The slope of three lines is the velocity of skyrmion center. (f) Schematic of phase transition for the skyrmion spin texture. The annihilation of skyrmion in phase space is similar to the Brownian motion in real space. Note that the Brownian particle is implemented as random hops between its equilibrium sites, the annihilation of skyrmion can also be treated as random hops between local energy minimum position, which is described by the Arrhenius' law and ΔE is the annihilation energy of isolated skyrmion. Take a Néel skyrmion in Fe/Ir for an example: (g) the Arrhenius' plots of skyrmion lifetime $1/\tau$ against the background temperature T_C/T ($T_C \sim 300$ K) with ($\mathcal{H}_{S+L}$) and without ($\mathcal{H}_S$) LLDF, in the cases of (g) $\lambda = 19.09$ Å and (h) $\lambda = 26.72$ Å.

simulation, $E_m \sim 20k_B = 1.72$ meV for Fe/Ir(111) and $E_m \sim 10k_B = 0.86$ meV for MnGe. For a given LLDF by fixing λ in SLD simulations, increasing the strength of current $\mathcal{J} = |\boldsymbol{\mathcal{J}}|$ can cut down E_m, thus reducing the dragging effects of LLDF. As shown in Fig. 6(d), for $\mathcal{J} = 2.23 \times 10^8$ A/m^2 applied, E_m owed to the LLDF is too large to get a significant drift motion of spin texture in $\mathcal{H}_{S+L}$. Correspondingly, without LLDF, it can move along the track under the same current $\mathcal{J}$ in $\mathcal{H}_S$. Raising $\mathcal{J}$ up to be 34.3×10^8 A/m^2, owed to LLDF, E_m is reduced significantly as shown in Fig. 6(c), so that the skyrmion transport speed in $\mathcal{H}_{S+L}$ is smaller than that in $\mathcal{H}_S$. Further increasing $\mathcal{J}$ to be 103×10^8 A/m^2 will flatten E_m, LLDF thus has little influence on spin texture transport, giving rise to the same drift motion of spin texture for both $\mathcal{H}_{S+L}$ and $\mathcal{H}_S$ as shown in Fig. 6(b). Similar simulation results of such a nonlinear skyrmion transport behavior were already reported in our previous study [17], which well demonstrates the effects of LLDF. On the other hand, for a given $\mathcal{J} = 34.3 \times 10^8$ A/m^2 applied, increasing λ would reduce the LLDF strength, thus decreasing the dragging effects on spin texture transport, which can be seen from the simulation results plotted in Fig. 6(e). In this regard, the presence of LLDF indeed affects the transport behavior of skyrmion spin texture. A stronger LLDF results in a larger dragging effect, which is significant in the cases of a weak field applied.

B. Effect of LLDF on skyrmion stability

Further, we investigate the manner in which LLDF disrupts the stability of the skyrmion by setting topological charges Q as the generalized coordinate in the phase space, whose evolution is described by Eq. (33). The system moving from $Q = 1$ to 0 denotes the annihilation of a single skyrmion spin texture to the ferromagnetic (FM) state. Because of the topological protection, it requires the system to go over an energy barrier for the skyrmion annihilation. Figure 6(a) illustrates the physical picture of the annihilation of a single Néel skyrmion spin texture of Fe/Ir embedded into the FM background under the thermal assistance, which is equivalent to the system moving from $Q = 1$ to 0 in the phase space. The skyrmion lifetime τ is used to characterize its stability, and it

TABLE II. Values of ΔE and τ_0 obtained by our simulation.

		ΔE [meV]	$1/\tau_0$ [$\times 10^{12}$ s^{-1}]
Ref. [53]	$\mathcal{H}_S$	166.00	$\sim$ 10.00
$\lambda = 19.09$ Å	$\mathcal{H}_S$	99.55	64.52
	$\mathcal{H}_{S+L}$	85.93	162.07
$\lambda = 26.72$ Å	$\mathcal{H}_S$	3.87	3.69
	$\mathcal{H}_{S+L}$	4.09	4.57

can be described by the Arrhenius' law as [52,53]

$$\frac{1}{\tau} = \frac{1}{\tau_0} \exp\left(-\frac{\Delta E}{k_B T}\right). \tag{34}$$

Here, T is the background temperature, ΔE is the energy barrier owed to the topological protection, which exists regardless of the presence of LLDF. Based on Eq. (34), we perform SLD simulations and estimate the values of τ_0 and ΔE in the cases with ($\mathcal{H}_{S+L}$) and without ($\mathcal{H}_S$) LLDF, respectively, to discuss the effects of LLDF on the skyrmion stability.

Here are the simulation details for investigating the skyrmion stability. Firstly, a single skyrmion in the given Fe/Ir system is generated under an appropriate external magnetic field H_{ext} within a wide temperature range. For instance, a single skyrmion with $\lambda = 5a = 19.09$ Å can be observed under $H_{\text{ext}} \sim 17.36 \times 10^{-3}$ T and $120\,\text{K} < T < 170\,\text{K}$. On the other hand, the one with $\lambda = 7a = 26.72$ Å is observed under $H_{\text{ext}} \sim 22.07 \times 10^{-3}$ T and $10\,\text{K} < T < 20\,\text{K}$. Here, $a = 3.818$ Å is the lattice constant of Fe/Ir system. Secondly, the system will relax by fixing the applied field H_{ext} at a preset temperature, so that the skyrmion undergoes an annihilation process. The time interval $t_n(T)$ for topological charge Q changing from 1 to 0 will be recorded. For each case, simulation of skyrmion annihilation will be repeated at least $n = 50$ times, so that the skyrmion lifetime $\tau(T)$ is evaluated as the mathematical expectation of t_n as $\tau(T) = \langle t_n(T)\rangle$. The logarithm form of the skyrmion lifetime under the certain temperature is proved to obey the Lorentz distribution [54] and the full width at half maximum is chosen to represent the error margin.

Figures 6(f)–6(h) present the simulation results of skyrmion lifetime with and without LLDF. It is found that the estimated temperature dependence of skyrmion lifetime well obeys the Arrhenius law of Eq. (34). Therefore, the values of ΔE and τ_0 can be obtained by fitting the simulation data in accordant with Eq. (34), which are listed in Table II. As plotted in Fig. 6(b), τ of $\mathcal{H}_{S+L}$ has an order of magnitude smaller than that of $\mathcal{H}_S$. Following Eq. (34), this reduction is arising from the enhancement of thermal fluctuation owed to LLDF, giving rise to a higher attempt frequency (i.e., $1/\tau_0$) for the system escaping out of the potential well near $Q = 1$ (i.e., $1/\tau_0 \sim 64.52 \times 10^{12}\,\text{s}^{-1}$ in $\mathcal{H}_S$ and $1/\tau_0 \sim 162.07 \times 10^{12}\,\text{s}^{-1}$ in $\mathcal{H}_{S+L}$), and the energy barrier ΔE is affected slightly by LLDF (i.e., $\sim$99.55 meV in $\mathcal{H}_S$ and $\sim$85.93 meV in $\mathcal{H}_{S+L}$). This confirms that LLDF exerts a negative effect on the stability of the skyrmion by altering the attempt frequency f_0. These conclusions drawn from our results are consistent with the previous studies [55–57]. Furthermore, increasing λ will decrease the LLDF strength and its effects on τ. This is well demonstrated in Fig. 6(h), where the simulation results of $\mathcal{H}_{S+L}$ are almost the same with those of $\mathcal{H}_S$ when $\lambda = 26.7$ Å. In this section, we can conclude that LLDF breaks the skyrmion ability by changing the attempt frequency $1/\tau_0$.

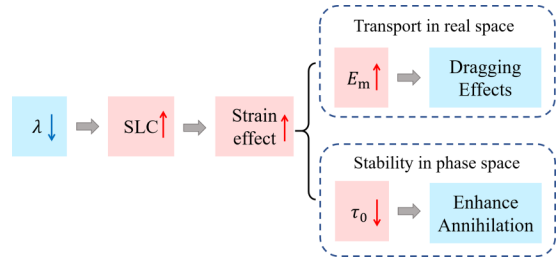

FIG. 7. The outline of the influence from SLC to the LLDF, and the resulting effects on spin texture evolution behavior.

To sum up, LLDF gives rise to significant effects on the evolution of skyrmion as outline as in Fig. 7. For the skyrmion transport, LLDF exerted an energy barrier so to provide negative dragging actions to the spin texture transport in real space, that decreasing size of the skyrmion indicates to enhance the SLC, which induces reinforced LLDF, thus hindering the skyrmion motion. For the skyrmion stability, the presence of LLDF enhances the thermal fluctuation, which helps the spin texture of skyrmion to break down its topological protection so to reduce its lifetime. Furthermore, decreasing size of the skyrmion indicates an enhancement of the SLC, which induces reinforced LLDF, thus hindering the skyrmion motion and devastating the stability of skyrmion. Note that all these effects occur in a defect-free chiral magnetic system. That is why we insist that the spin texture is just one-side of the skyrmion "coin", and the LLDF is the other side. Both sides will have intrinsic interaction in the skyrmion evolution and reveal complicated nonlinear and nonadiabatic coupling effects.

IV. CONCLUSIONS

In this paper, we perform the microdynamic analysis on the magnetic-mechanical effects in skyrmion materials. As one of the microdynamic sources, spin-lattice coupling induces the intrinsic nonlinear irrational strain field (named local lattice distortion field, LLDF) with the spiral spin texture, both of which are the two integral parts of skyrmion microstructure. An analytical formulation of LLDF was then proposed, whose strength and morphology are determined by the magnetic-mechanical competition and the skyrmion size. The atomistic simulation results based on spin-lattice dynamics confirmed our conjecture. Furthermore, effects of LLDF on the transport and stability of skyrmion spin texture were found to be significant, which suggests it could not be neglected when studying the dynamical evolution behaviors of skyrmion and its functional application in spintronic devices.

ACKNOWLEDGMENTS

This work was supported by the National Natural Science Foundation of China (NSFC) (Grants No. 12132020

and No. 12002400), Guangdong Basic and Applied Basic Research Foundation (Grant No. 2022A1515010249), and Guangdong Provincial Key Laboratory of Magnetoelectric Physics and Devices (Grant No. 2022B1212010008). The simulations were performed on resources provided by the National Supercomputer Center in Guangzhou and the Centre for Physical Mechanics and Biophysics in School of Physics in Sun Yat-Sen University.

APPENDIX: THE DEDUCTION OF INTERATOMIC FORCE

From the Hamiltonian $\mathcal{H}$ in Eq. (1) for the spin-lattice coupling system, the interatomic force $\boldsymbol{f}_{ij}$ between the ith and jth atoms is derived as

$$\begin{aligned}\boldsymbol{f}_{ij} &= -\nabla\mathcal{H}_{S+L} = (-\nabla\mathcal{H}_L) + (-\nabla\mathcal{H}_J) + (-\nabla\mathcal{H}_D)\\ &\equiv \boldsymbol{f}^L_{ij} + \boldsymbol{f}^J_{ij} + \boldsymbol{f}^D_{ij},\end{aligned} \tag{A1}$$

where $\nabla\mathcal{H} \equiv \frac{\partial\mathcal{H}}{\partial \boldsymbol{r}_{ij}}$; $\boldsymbol{f}^L_{ij}$, $\boldsymbol{f}^J_{ij}$, and $\boldsymbol{f}^D_{ij}$ are the parts of $\boldsymbol{f}_{ij}$ arising from $\mathcal{H}_L$, $\mathcal{H}_J$, and $\mathcal{H}_D$, respectively. Note that there is an identity for an arbitrary X as function of r_{ij} as

$$\nabla X \equiv \frac{\partial X}{\partial \boldsymbol{r}_{ij}} = (\nabla r_{ij})\frac{\partial X}{\partial r_{ij}} \equiv \hat{r}_{ij}X'(r_{ij}), \tag{A2}$$

where $X'(r_{ij}) \equiv \frac{\partial X}{\partial r_{ij}}$. Therefore,

$$\boldsymbol{f}^L_{ij} = -\nabla\mathcal{H}_L = -\hat{r}_{ij}\frac{\partial\mathcal{H}_L}{\partial r_{ij}} = -\hat{r}_{ij}U'(r_{ij}). \tag{A3}$$

Similarly,

$$\boldsymbol{f}^J_{ij} = -\nabla\mathcal{H}_J = \hat{r}_{ij}(\boldsymbol{S}_i\cdot\boldsymbol{S}_j)J'(r_{ij}) \equiv \boldsymbol{\varphi}_{ij}J'(r_{ij}), \tag{A4}$$

where $\boldsymbol{\varphi}_{ij} \equiv \hat{r}_{ij}(\boldsymbol{S}_i\cdot\boldsymbol{S}_j)$. Thirdly,

$$\begin{aligned}\boldsymbol{f}^D_{ij} &= -\nabla\mathcal{H}_D = -\nabla[D(r_{ij})\hat{r}_{ij}\cdot\boldsymbol{A}_{ij}]\\ &= -\nabla\left[\left(\frac{D(r_{ij})}{r_{ij}}\right)(\boldsymbol{r}_{ij}\cdot\boldsymbol{A}_{ij})\right]\\ &= (\boldsymbol{r}_{ij}\cdot\boldsymbol{A}_{ij})\nabla\left(\frac{D(r_{ij})}{r_{ij}}\right) + \left(\frac{D(r_{ij})}{r_{ij}}\right)\nabla(\boldsymbol{r}_{ij}\cdot\boldsymbol{A}_{ij}).\end{aligned} \tag{A5}$$

Here,

$$\begin{aligned}\nabla\left(\frac{D(r_{ij})}{r_{ij}}\right) &= \frac{1}{r_{ij}}\nabla D + D\nabla\left(\frac{1}{r_{ij}}\right)\\ &= \frac{\hat{r}_{ij}}{r_{ij}}D'(r_{ij}) - \frac{D(r_{ij})\hat{r}_{ij}}{r^2_{ij}}\\ &= \frac{\hat{r}_{ij}}{r_{ij}}\left(D'(r_{ij}) - \frac{D(r_{ij})}{r_{ij}}\right)\end{aligned} \tag{A6}$$

and

$$\begin{aligned}\nabla(\boldsymbol{r}_{ij}\cdot\boldsymbol{A}_{ij}) &= (\boldsymbol{r}_{ij}\cdot\nabla)\boldsymbol{A}_{ij} + (\boldsymbol{A}_{ij}\cdot\nabla)\boldsymbol{r}_{ij}\\ &\quad + \boldsymbol{r}_{ij}\times(\nabla\times\boldsymbol{A}_{ij}) + \boldsymbol{A}_{ij}\times(\nabla\times\boldsymbol{r}_{ij})\\ &= (\boldsymbol{A}_{ij}\cdot\nabla)\boldsymbol{r}_{ij} = \boldsymbol{A}_{ij},\end{aligned} \tag{A7}$$

where we use the fact that $\boldsymbol{A}_{ij}$ is independent of $\boldsymbol{r}_{ij}$ because $\boldsymbol{S}_i$ and $\boldsymbol{r}_i$ are independent degrees of freedom in our spin-lattice coupled system, and $\nabla\times\boldsymbol{r}_{ij} \equiv 0$. Substituting Eqs. (A6) and (A7) into Eq. (A5), we can get

$$\begin{aligned}\boldsymbol{f}^D_{ij} &= (\boldsymbol{r}_{ij}\cdot\boldsymbol{A}_{ij})\frac{\hat{r}_{ij}}{r_{ij}}\left(D'(r_{ij}) - \frac{D(r_{ij})}{r_{ij}}\right) + \left(\frac{D(r_{ij})}{r_{ij}}\right)\boldsymbol{A}_{ij}\\ &= (\hat{r}_{ij}\cdot\boldsymbol{A}_{ij})\hat{r}_{ij}D'(r_{ij}) + \frac{D(r_{ij})}{r_{ij}}(\boldsymbol{A}_{ij} - (\hat{r}_{ij}\cdot\boldsymbol{A}_{ij})\hat{r}_{ij}).\end{aligned} \tag{A8}$$

Accordingly, we have another identity for an arbitrary vector $\boldsymbol{A}_{ij}$ with respect to $\hat{r}_{ij}$, that

$$\boldsymbol{A}_{ij} = \boldsymbol{A}^{\parallel}_{ij} + \boldsymbol{A}^{\perp}_{ij}, \tag{A9}$$

where $\boldsymbol{A}^{\parallel}_{ij}$ and $\boldsymbol{A}^{\perp}_{ij}$ are the $\boldsymbol{A}_{ij}$ components parallel and perpendicular to the reference direction $\hat{r}_{ij}$, and

$$\boldsymbol{A}^{\parallel}_{ij} = (\hat{r}_{ij}\cdot\boldsymbol{A}_{ij})\hat{r}_{ij}, \quad \boldsymbol{A}^{\perp}_{ij} = (\hat{r}_{ij}\times\boldsymbol{A}_{ij})\times\hat{r}_{ij}. \tag{A10}$$

Therefore, $\boldsymbol{f}^D_{ij}$ reads

$$\boldsymbol{f}^D_{ij} = \boldsymbol{A}^{\parallel}_{ij}D'(r_{ij}) + \boldsymbol{A}^{\perp}_{ij}D(r_{ij})/r_{ij}. \tag{A11}$$

Finally, combining Eqs. (A1), (A3), (A4), and (A11), we have

$$\begin{aligned}\boldsymbol{f}_{ij} &= \boldsymbol{f}^L_{ij} + \boldsymbol{f}^J_{ij} + \boldsymbol{f}^D_{ij}\\ &= -\frac{\partial U}{\partial r_{ij}}\hat{r}_{ij} + \frac{\partial J}{\partial r_{ij}}\boldsymbol{\varphi}_{ij} + \frac{\partial D}{\partial r_{ij}}\boldsymbol{A}^{\parallel}_{ij} + \frac{D}{r_{ij}}\boldsymbol{A}^{\perp}_{ij}.\end{aligned} \tag{A12}$$

Here, Eq. (A12) is the Eq. (5) in the main text.

[1] S. Mühlbauer, B. Binz, F. Jonietz, C. Pfleiderer, A. Rosch, A. Neubauer, R. Georgii, and P. Böni, Skyrmion lattice in a chiral magnet, Science **323**, 915 (2009).

[2] N. Nagaosa and Y. Tokura, Topological properties and dynamics of magnetic skyrmions, Nat. Nanotechnol. **8**, 899 (2013).

[3] D. Bhowmik and S. Salahuddin, Deterministic spin–orbit torque switching of a perpendicularly polarized magnet using wedge shape of the magnet, SPIN **06**, 1640008 (2016).

[4] F. Wang, X. Zhang, Z. Zhang, and Y. Liu, Deterministic magnetization switching by spin–orbit torque in a ferromagnet with tilted magnetic anisotropy: A macrospin modeling, J. Magn. Magn. Mater. **527**, 167757 (2021).

[5] J. Iwasaki, M. Mochizuki, and N. Nagaosa, Current-induced skyrmion dynamics in constricted geometries, Nat. Nanotechnol. **8**, 742 (2013).

[6] S. S. Parkin, M. Hayashi, and L. Thomas, Magnetic domain-wall racetrack memory, Science **320**, 190 (2008).

[7] A. Fert, V. Cros, and J. Sampaio, Skyrmions on the track, Nat. Nanotechnol. **8**, 152 (2013).

[8] J. Seidel, R. K. Vasudevan, and N. Valanoor, Topological structures in multiferroics–domain walls, skyrmions and vortices, Adv. Electron. Mater. **2**, 1500292 (2016).

[9] X. Xing, P. W. T. Pong, and Y. Zhou, Skyrmion domain wall collision and domain wall-gated skyrmion logic, Phys. Rev. B **94**, 054408 (2016).

[10] X. Zhang, Y. Zhou, M. Ezawa, G. Zhao, and W. Zhao, Magnetic skyrmion transistor: Skyrmion motion in a voltage-gated nanotrack, Sci. Rep. **5**, 11369 (2015).

[11] S. I. Kiselev, J. Sankey, I. Krivorotov, N. Emley, R. Schoelkopf, R. Buhrman, and D. Ralph, Microwave oscillations of a nanomagnet driven by a spin-polarized current, Nature (London) **425**, 380 (2003).

[12] P. Braganca, B. Gurney, B. Wilson, J. Katine, S. Maat, and J. Childress, Nanoscale magnetic field detection using a spin torque oscillator, Nanotechnology **21**, 235202 (2010).

[13] N. S. Kiselev, A. Bogdanov, R. Schäfer, and U. Rößler, Chiral skyrmions in thin magnetic films: New objects for magnetic storage technologies? J. Phys. D **44**, 392001 (2011).

[14] P.-W. Ma, C. H. Woo, and S. L. Dudarev, Large-scale simulation of the spin-lattice dynamics in ferromagnetic iron, Phys. Rev. B **78**, 024434 (2008).

[15] H. Wang, P.-W. Ma, and C. H. Woo, Exchange interaction function for spin-lattice coupling in bcc iron, Phys. Rev. B **82**, 144304 (2010).

[16] Y. Wu, H. Wen, J. Liu, K. Lai, and Y. Zheng, Atomistic simulations of spin-lattice coupling effects on magnetomechanics in skyrmion materials, Phys. Rev. B **100**, 144310 (2019).

[17] Y. Wu, H. Wen, W. Chen, and Y. Zheng, Microdynamic study of spin-lattice coupling effects on skyrmion transport, Phys. Rev. Lett. **127**, 097201 (2021).

[18] Y. Hu, X. Wan, and B. Wang, Thermodynamics of magnetic emergent crystals under coupled magnetoelastic fields, New J. Phys. **23**, 023016 (2021).

[19] Y. Hu, Emergent elasticity and topological stability of solitons, arXiv:2208.14916.

[20] I. Turek, J. Kudrnovský, V. Drchal, and P. Bruno, Exchange interactions, spin waves, and transition temperatures in itinerant magnets, Philos. Mag. **86**, 1713 (2006).

[21] J. Chen, W. Cai, M. Qin, S. Dong, X. Lu, X. Gao, and J.-M. Liu, Helical and skyrmion lattice phases in three-dimensional chiral magnets: Effect of anisotropic interactions, Sci. Rep. **7**, 7392 (2017).

[22] I. Dzyaloshinsky, A thermodynamic theory of "weak" ferromagnetism of antiferromagnetics, J. Phys. Chem. Solids **4**, 241 (1958).

[23] T. Moriya, Anisotropic superexchange interaction and weak ferromagnetism, Phys. Rev. **120**, 91 (1960).

[24] F. Keffer, Moriya interaction and the problem of the spin arrangements in β MnS, Phys. Rev. **126**, 896 (1962).

[25] A. Fert, *Materials Science Forum* (Trans Tech Pub., Zurich, 1990), Vol. 59, pp. 439–480.

[26] F. Hellman, A. Hoffmann, Y. Tserkovnyak, G. S. D. Beach, E. E. Fullerton, C. Leighton, A. H. MacDonald, D. C. Ralph, D. A. Arena, H. A. Dürr *et al.*, Interface-induced phenomena in magnetism, Rev. Mod. Phys. **89**, 025006 (2017).

[27] A. Fert and P. M. Levy, Role of anisotropic exchange interactions in determining the properties of spin-glasses, Phys. Rev. Lett. **44**, 1538 (1980).

[28] A. N. Bogdanov and C. Panagopoulos, Physical foundations and basic properties of magnetic skyrmions, Nat. Rev. Phys. **2**, 492 (2020).

[29] L. B. Drissi, E. H. Saidi, M. Bousmina, and O. Fassi-Fehri, in *Magnetic Skyrmions*, edited by D. R. Sahu (IntechOpen, Rijeka, 2021), Chap. 1.

[30] See Supplemental Material at http://link.aps.org/supplemental/10.1103/PhysRevB.109.104427 for the analytical deduction of LLDF morphology, starting from the general expression of spin texture of a single skyrmion, and the atomic force in a magnetic system provided by the radial and tangential neighboring atoms.

[31] C. Feng, F. Meng, Y. Wang, J. Jiang, N. Mehmood, Y. Cao, X. Lv, F. Yang, L. Wang, Y. Zhao *et al.*, Field-free manipulation of skyrmion creation and annihilation by tunable strain engineering, Adv. Funct. Mater. **31**, 2008715 (2021).

[32] Y. Tokura and N. Kanazawa, Magnetic skyrmion materials, Chem. Rev. **121**, 2857 (2021).

[33] V. V. Brazhkin, L. N. Dzhavadov, and F. S. El'kin, Study of the compressibility of FeSi, MnSi, and CoS_2 transition-metal compounds at high pressures, JETP Lett. **104**, 99 (2016).

[34] J. F. DiTusa, S. B. Zhang, K. Yamaura, Y. Xiong, J. C. Prestigiacomo, B. W. Fulfer, P. W. Adams, M. I. Brickson, D. A. Browne, C. Capan, Z. Fisk, and J. Y. Chan, Magnetic, thermodynamic, and electrical transport properties of the noncentrosymmetric B 20 germanides MnGe and CoGe, Phys. Rev. B **90**, 144404 (2014).

[35] H. Takizawa, T. Sato, T. Endo, and M. Shimada, High-pressure synthesis and electrical and magnetic properties of MnGe and CoGe with the cubic B20 structure, J. Solid State Chem. **73**, 40 (1988).

[36] A. S. Ahmed, B. D. Esser, J. Rowland, D. W. McComb, and R. K. Kawakami, Molecular beam epitaxy growth of [CrGe/MnGe/FeGe] superlattices: Toward artificial B20 skyrmion materials with tunable interactions, J. Cryst. Growth **467**, 38 (2017).

[37] J. Pulikkotil, S. Auluck, P. Rout, and R. Budhani, Effect of pressure on itinerant magnetism and spin disorder in cubic FeGe, J. Phys.: Condens. Matter **24**, 096003 (2012).

[38] L. Xu, H. Han, J. Fan, D. Shi, D. Hu, H. Du, L. Zhang, Y. Zhang, and H. Yang, Magnetic entropy change and accurate determination of Curie temperature in single-crystalline helimagnet FeGe, Europhys. Lett. **117**, 47004 (2017).

[39] H. P. Singh, Determination of thermal expansion of germanium, rhodium and iridium by x-rays, Acta Cryst. A: Cryst. Phys. Diffr. Theor. Gen. Crystallogr. **24**, 469 (1968).

[40] Y. Cerenius and L. Dubrovinsky, Compressibility measurements on iridium, J. Alloys Compd. **306**, 26 (2000).

[41] W.-H. Chen, P.-C. Jiang, C.-Y. Hsieh, and J.-S. Tsay, Structure related magnetic dead layer for ultrathin Fe/Ir (111) films, IEEE Trans. Magn. **50**, 1 (2014).

[42] D. E. Laughlin, Magnetic transformations and phase diagrams, Metall. Mater. Trans. A **50**, 2555 (2019).

[43] L. Liu, C.-F. Pai, Y. Li, H. Tseng, D. Ralph, and R. Buhrman, Spin-torque switching with the giant spin Hall effect of tantalum, Science **336**, 555 (2012).

[44] J. Li, A. Tan, K. Moon, A. Doran, M. Marcus, A. Young, E. Arenholz, S. Ma, R. Yang, C. Hwang *et al.*, Tailoring the

topology of an artificial magnetic skyrmion, Nat. Commun. **5**, 4704 (2014).

[45] S. Heinze, K. Von Bergmann, M. Menzel, J. Brede, A. Kubetzka, R. Wiesendanger, G. Bihlmayer, and S. Blügel, Spontaneous atomic-scale magnetic skyrmion lattice in two dimensions, Nat. Phys. **7**, 713 (2011).

[46] N. Hatano and M. Suzuki, in *Quantum Annealing and Other Optimization Methods* (Springer, New York, 2005), pp. 37–68.

[47] P.-W. Ma and C. H. Woo, Parallel algorithm for spin and spin-lattice dynamics simulations, Phys. Rev. E **79**, 046703 (2009).

[48] L. Liu, W. Chen, and Y. Zheng, Flexoresponses of synthetic antiferromagnetic systems hosting skyrmions, Phys. Rev. Lett. **128**, 257201 (2022).

[49] J. Wang, Mechanical control of magnetic order: From phase transition to skyrmions, Annu. Rev. Mater. Res. **49**, 361 (2019).

[50] H. A. Kramers, Brownian motion in a field of force and the diffusion model of chemical reactions, Physica **7**, 284 (1940).

[51] A. Thiele, Steady-state motion of magnetic domains, Phys. Rev. Lett. **30**, 230 (1973).

[52] K. J. Laidler, The development of the Arrhenius equation, J. Chem. Educ. **61**, 494 (1984).

[53] S. von Malottki, P. F. Bessarab, S. Haldar, A. Delin, and S. Heinze, Skyrmion lifetime in ultrathin films, Phys. Rev. B **99**, 060409(R) (2019).

[54] A. K. Tagantsev, I. Stolichnov, N. Setter, J. S. Cross, and M. Tsukada, Non-Kolmogorov-Avrami switching kinetics in ferroelectric thin films, Phys. Rev. B **66**, 214109 (2002).

[55] M. Hoffmann, G. P. Müller, and S. Blügel, Atomistic perspective of long lifetimes of small skyrmions at room temperature, Phys. Rev. Lett. **124**, 247201 (2020).

[56] J. Wild, T. N. Meier, S. Pöllath, M. Kronseder, A. Bauer, A. Chacon, M. Halder, M. Schowalter, A. Rosenauer, J. Zweck *et al.*, Entropy-limited topological protection of skyrmions, Sci. Adv. **3**, e1701704 (2017).

[57] R. E. Troncoso and Á. S. Núñez, Brownian motion of massive skyrmions in magnetic thin films, Ann. Phys. **351**, 850 (2014).